1

Introduction

1

1.1. Hot astrophysical plasmas in X-rays

Hot astrophysical plasmas pervade the Universe: about half of the baryonic content in the Universe is expected to have a temperature of $T > 10^5$ K, which is largely undetectable by observational facilities at wavelength longer than X-rays (0.1–100 Å). The X-ray band therefore provides unique opportunities to find clues to answer major astrophysical questions like "How does AGN feedback influence the host galaxies and beyond?" and "What is the chemical composition of the Universe and what are the origins of these elements?".

X-ray spectroscopy enables us to constrain physical properties (temperature, density, abundance, microscopic turbulence, line of sight velocity, etc.) of these hot plasmas. Thanks to the grating spectrometers aboard *XMM-Newton* (den Herder et al. 2001; Mason et al. 2001; Strüder et al. 2001) and *Chandra* (Brinkman et al. 2000; Canizares et al. 2005), our knowledge of the hot and energetic Universe has advanced in the past two decades. We are also looking forward to new missions like *Arcus* (Smith et al. 2016), *Astro-H* (also known as *Hitomi*, Takahashi et al. 2014), and *Athena* (Nandra et al. 2013), which are built on new technologies. Compared to the current generation of spectrometers, the next generation improves the spectral resolution by one or two orders of magnitude so that blended spectral features can be clearly resolved.

High quality spectra from both current and future generations of X-ray spectrometers challenge plasma models that are widely used in the community. More accurate and complete atomic data are required to build better plasma models. Otherwise, the interpretation of the physical properties of the plasmas might be incorrect.

When I started my PhD project in 2014, the *Hitomi* satellite was scheduled to be launched in 2016. There was and still is an urgent need for improvements on the SPEX code. SPEX is a software package, including atomic data and various plasma models, designed for the analysis and interpretation of high-resolution cosmic X-ray spectra. My first project was to update the radiative recombination data in the SPEX code. Radiative recombination is a fundamental atomic process, therefore, almost all plasma models are affected by the accuracy and completeness of the radiative recombination data. We aimed to test the updated SPEX code by measuring the chemical abundances in the CHEERS sample (de Plaa et al. 2017) of clusters observed with *XMM-Newton* at that time and apply to *Hitomi* data when they are available.

While I made progresses on updating the radiative recombination data in SPEX

and commenced on studying the nitrogen enrichment of the CHEERS sample in my second year as a PhD student, *Hitomi* spun out of control about forty days after its successful launch. Although I did not work directly on the Perseus spectra observed with the Soft X-ray Spectrometer aboard *Hitomi*, the updated collisional ionization plasma model in the SPEX code has been applied to the Perseus spectra which lead to several high profile publications (e.g., Hitomi Collaboration et al. 2017a,b). I decided to shift my focus to Active Galactic Nuclei (AGN) since there are still many interesting questions to be answered with photoionization modeling of high-resolution X-ray spectra of AGN obtained with the current generation of spectrometers aboard *Chandra* and *XMM-Newton*. For instance, it was recently discovered that some Seyfert 1 galaxies have a special type of photoionized outflow, which heavily obscures the soft X-ray continuum and causes simultaneous deep, broad UV absorption troughs (e.g., Kaastra et al. 2014; Mehdipour et al. 2017). As a result, X-ray narrow emission lines stand out above the diminished continuum. Such a special state of the AGN offers a unique opportunity to study relatively weak narrow emission lines in the soft X-ray band that are previously hidden by the unobscured continuum.

1.2. Active Galactic Nuclei and circumnuclear media

The center of almost every galaxy, except for the smallest ones, contains a supermassive black hole (SMBH) with $M_{\rm BH} > 10^5$ $\rm M_\odot$. The growth of the supermassive black hole is realized via accretion of matter. When the accretion rate is above a certain limit ($\gtrsim 10^{-5}$ Eddington ratio), the central region of this active galaxy is called an active galactic nucleus (AGN). The rich phenomenology of AGN, covering the entire electromagnetic spectrum, is intriguing yet puzzling. This is evident because even the number of acronyms or classes related to AGN has exceeded a dozen and each reveals certain aspects of the nature of AGN.

Seyfert galaxies (Seyfert 1943) are one of the two largest groups of AGN, along with quasars (Schmidt 1963). Seyferts, accounting for about 10% of all galaxies (Maiolino & Rieke 1995), are thought to be powered by the same mechanism that occurs in quasars, but Seyferts are closer (thus brighter) and less luminous than quasars. Quasars are also known as quasi-stellar objects (QSOs). The former term originally requires radio detection (no longer required now, Padovani et al. 2017), while the latter refers to a quasar-like, non-radio source. If its ratios of radio (5 GHz)

to optical (B-band) flux $F_5/F_B \gtrsim 10$ (Kellermann et al. 1989), the AGN is radio-loud (RL). Otherwise, it is radio quiet (RQ). Nevertheless, Padovani et al. (2017) made a convincing plea to abandon the RL and RQ terms, replacing them with "jetted" and "non-jetted" since the two classes are intrinsically different.

In terms of optical spectral features, Seyfert galaxies are first divided into two subgroups (Weedman 1973). Seyfert 1 galaxies possess broad permitted emission lines with a velocity broadening of a few 10^3 km s^{-1} and narrow forbidden emission lines with a velocity broadening of a few 10^2 km s^{-1}, while Seyfert 2 galaxies only have narrow permitted and forbidden emission lines. Later, Osterbrock (1981) introduced the notations Seyfert 1.5, 1.8 and 1.9, where the subclasses are again based on the optical appearance of the spectrum, with the numerically larger subclasses having weaker broad lines relative to the narrow lines. The commonly used term Type I/II applies to both Seyferts and quasars, based on their optical spectra features described above.

It is also possible that the optical spectrum is relatively featureless. Blazars are a type of AGN that show rapid variability, high polarization and a relatively featureless spectrum.

It is important to emphasize that the aforementioned acronyms or (sub)classes cover merely the most frequently used ones, a more complete list can be found in a recent review by Padovani et al. (2017). Regardless of the variety of naming, most AGN include several of the following components (Figure 1.1):

1. Accretion disk: a rotation-dominated accretion flow, typically at a sub-parsec scale. A corona of hot plasma might sit above the centre of the accretion disk and produces photons at hard X-ray energies via inverse-Compton scattering (Haardt & Maraschi 1991, 1993).

2. Broad-line region (BLR): a high-density, high-velocity ($v \gtrsim 10^3$ km s^{-1}) and dust-free plasma. The BLR is about a few light-days to light-weeks away from the black hole (Peterson et al. 2004).

3. Torus: an axisymmetric dusty structure with its inner boundary about 0.01–1 pc, which is about four times the Blamer line BLR (Koshida et al. 2014).

4. Narrow-line region (NLR): a low-density and low-velocity ($v \lesssim 10^3$ km s^{-1}) plasma. The NLR extends from the outer edge of the torus to at least a few parsec away (Bennert et al. 2006a,b), along the ionization cone.

5. Outflows: feedback in the radiative mode (wind) or radio mode (jet).

It is important to understand the physics of inflows and outflows associated with AGN, thus, the evolution of SMBHs, the regulated evolution of the host galaxies and the origin of the circumnuclear media (for recent reviews see Fabian 2012; Kormendy & Ho 2013; Netzer 2015).

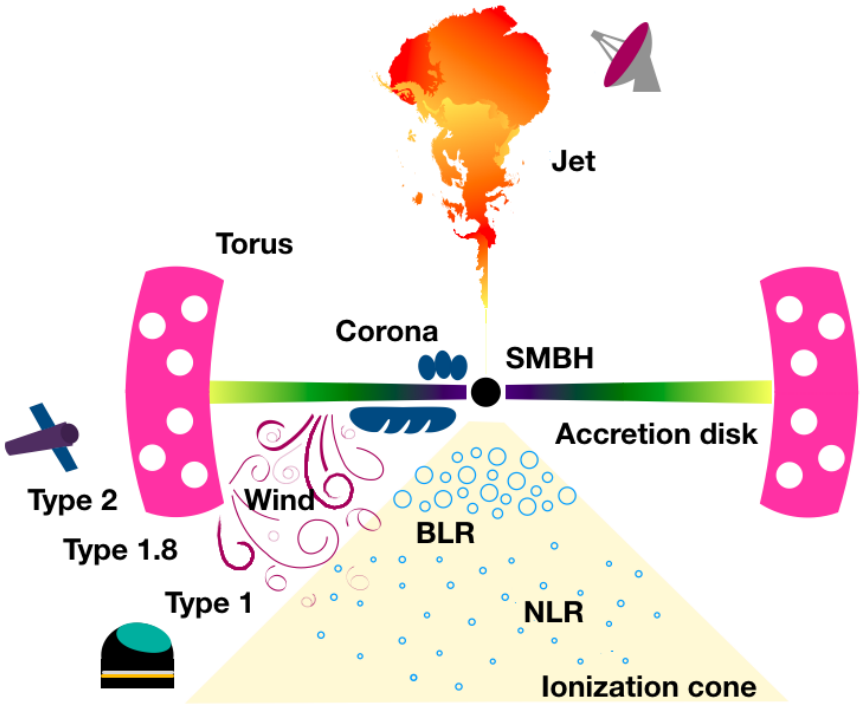

Figure 1.1: A sketch of the main components in active galactic nuclei, including the supermassive black hole (SMBH), accretion disk, corona, broad-line region (BLR), dusty torus, narrow-line region (NLR), outflows (jet and wind).

The radiative mode of the AGN outflow (wind) is of particular interest here since there are significant gaps in our understanding of this outflow phenomenon. Whether the outflow plays an important role in the cosmic feedback is determined by the mass outflow rate and kinetic power carried by the outflow

$$\dot{M}_{\rm out} \propto n_{\rm H}\, v_{\rm out}\, r^2,\ L^{\rm KE}_{\rm out} = \frac{1}{2}\,\dot{M}_{\rm out}\, v^2_{\rm out}, \tag{1.1}$$

where $n_{\rm H}$ is the hydrogen number density of the outflow, $v_{\rm out}$ the outflow velocity and r the distance to the central engine (e.g., King & Pounds 2003). An accurate measurement of the distance of the outflow is the prerequisite of estimating $\dot{M}_{\rm out}$

and $L_{\rm out}^{\rm KE}$ (Equation 1.1). Unfortunately, circumnuclear media are often not spatially resolved with direct imaging. Distance can be indirectly measured via density:

$$\xi = \frac{L}{n_{\rm H}\, r^2} \tag{1.2}$$

where ξ is the ionization parameter of the outflow, L is the 1–1000 Ryd ionizing luminosity (Krolik et al. 1981; Tarter et al. 1969). Both the ionization parameter and ionizing luminosity are observable. Nevertheless, it is not trivial to determine the density of the photoionized outflow.

Three different approaches have been used to measure the density of AGN outflows. The first approach is a spectral analysis of density sensitive emission lines. It is well known that the ratio of intercombination to forbidden emission lines in the He-like triplets varies for plasmas with different density values (e.g., Porquet et al. 2010). This density probe, observed in the X-ray wavelength range, has been applied to a few AGNs, e.g., NGC 4051 (Collinge et al. 2001), NGC 4593 (McKernan et al. 2003), and NGC 4151 (Schurch et al. 2004), where the upper limits of the plasma density are derived. The density of circumnuclear media is orders of magnitude lower for the triplet line ratios to be effective, thus, only upper limits are obtained.

A second approach is a timing analysis where the response of the changing ionizing continuum is monitored. A high-density plasma recombines more rapidly, thus yields a shorter recombination timescale. This approach has been used to constrain the density in, for instance, Mrk 509 (Kaastra et al. 2012), NGC 5548 (Ebrero et al. 2016), and NGC 4051 (Silva et al. 2016). The timing analysis is challenging in general because it requires frequent (if not continuous) monitoring with adequately high-quality spectra to verify the response. Note that even if perfect observations were available for an ideal variable target, the maximum continuous observational window for some sources is typically less than 100 days due to the sky positions of the targets and the pointing constraints of the space observatories. This maximum continuous observational window determines the lowest density (10^{4-5} cm^{-3}) that can be probed via the timing analysis(Figure 1.2). In addition, if the plasma density is so low that the recombination timescale ($\tau_{\rm rec}$) is orders of magnitude higher than the variability timescale $\tau_{\rm var}$ of the ionizing continuum, the plasma is in a quasi-steady state (Nicastro et al. 1999). In other words, the ionization balance of the plasma varies slightly around the mean value corresponding to the mean ionizing flux level over time (Kaastra et al. 2012; Silva et al. 2016).

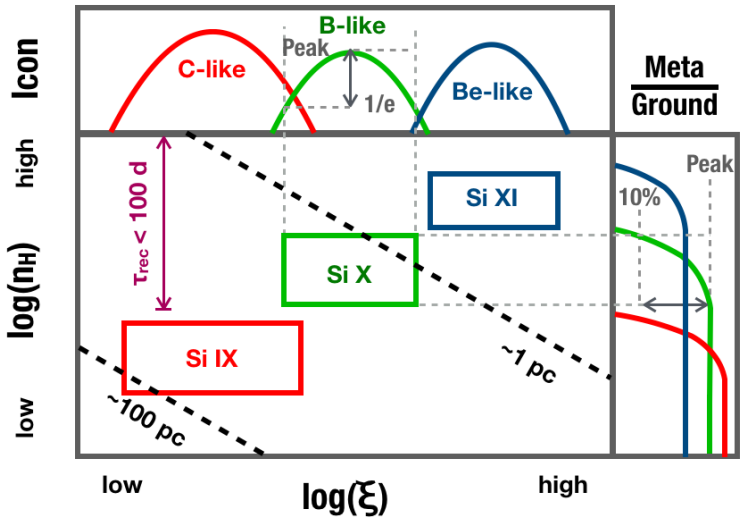

Figure 1.2: A sketch of the domain of density and ionization parameter where metastable absorption lines can be used for diagnostics in a photoionized plasma. Each box in the main plot corresponds to a certain ion. Within each box, plasma density and ionization parameter can be well constrained. Outside the box, only an upper or lower limit can be obtained. This is because the ion concentration ("Icon" in the upper plot) and the metastable to ground level population ratio (in the right plot) are too low. Dashed lines indicate the distance of the photoionized plasma with respect to the central engine. The limit of the timing analysis for the density measurement is also shown here.

The third approach is a spectral analysis where density sensitive metastable absorption lines are identified. A metastable level has a longer lifetime than ordinary excited levels and a shorter lifetime than the ground level. The line ratio of the metastable to ground absorption lines is determined by the level population ratio of the metastable to ground level, which, in turn, depend on the density of the plasma as the metastable level can be populated via collisional excitation from the ground level (Figures 1.3 and 1.4). This method has been successfully used for absorption lines observed in the UV band (e.g., Arav et al. 2015). In the X-ray band, either upper or lower limits have been obtained for a few AGNs, including Mrk 279 (Kaastra et al. 2004), NGC 4051 (King et al. 2012) and NGC 5548 (Mao et al. 2017b). This approach requires less observational time compared to the timing analysis. But current grating spectrometers on board *XMM-Newton* and *Chandra* lack spectral resolution and effective area to put tight constraints on the density. Future missions like *Arcus* (Smith et al. 2016) are required for such kind of analysis. Note that even if perfect instruments were available, for each ion, its ground and metastable lines can only be detected when the ionization parameter of the plasma falls in a

certain range and when the line ratio of the metastable to ground absorption lines is sensitive to a certain range of plasma densities (Figure 1.2). When all the ions are considered, there are still some uncovered regions in the density and ionization parameter space (Figure 7 in Mao et al. 2017b). Therefore, a timing analysis would be needed as a complementary approach.

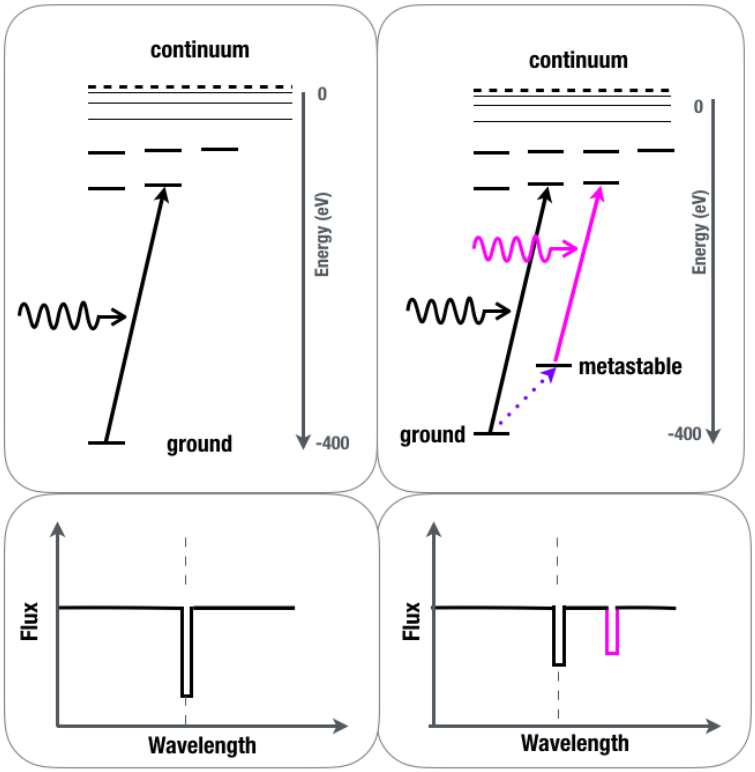

Figure 1.3: A sketch of ground and metastable absorption lines. The metastable level can be populated via collisional excitation from the ground level, thus the line ratio of the metastable to ground absorption lines is sensitive to the density of the plasma. The metastable level can also be populated via cascades from higher levels, but collisional excitation is the dominant process.

Apart from the density/distance of the outflow, there are more open questions concerning the circumnuclear media in active galactic nuclei. For instance, broad and narrow emission lines are observed in optical, UV and sometimes in X-rays, what are the physical properties and geometry of these emission line regions? More importantly, what is the origin of these emission line regions? And do these emission line regions relate to AGN outflows?

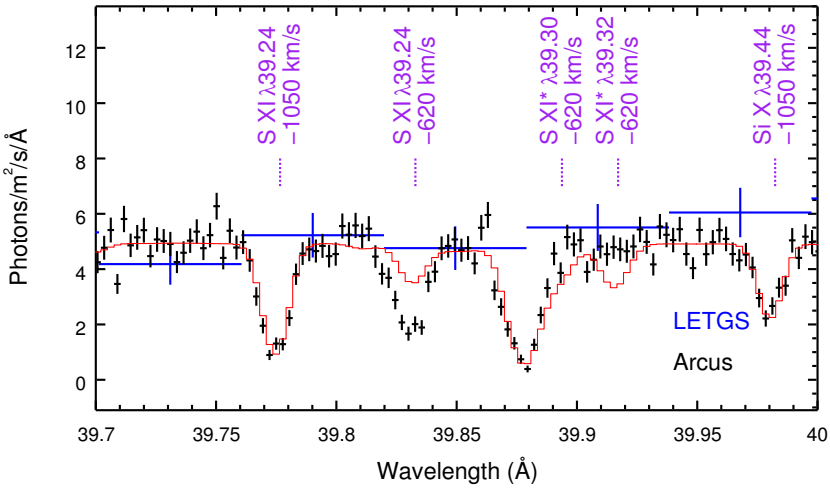

Figure 1.4: Observed *Chandra*/LETGS (in blue, with 345 ks exposure) spectrum of NGC 5548 in the neighbourhood of S XI (39.24 Å in the observed frame) and a 300 ks simulation of the same spectrum with *Arcus*. Two outflow components with different velocities are present here. The red solid line is a model with high density, while the simulated data (in black) corresponds to a lower density scenario. The metastable absorption lines are labelled with $\star$. More details can be found in Kaastra et al. (2017).

1.3. Intracluster media and chemical enrichment

Clusters of galaxies, also known as galaxy clusters, are the largest gravitational bound structures in the Universe. Galaxy clusters usually consist of hundreds to thousands member galaxies[1], with a total mass of 10^{14-15} $M_\odot$. A large fraction ($\sim 15-20$ %) of the total mass forms the hot ($kT \sim 10^{7-8}$ K) and X-ray emitting intracluster medium (ICM), while the visible member galaxies contribute merely $\sim 3-5$ %. The rest is dark matter (Schindler & Diaferio 2008).

Based on the radial temperature profile, galaxy clusters can be divided into two subclasses (Böhringer & Werner 2010): those with temperature profiles decreasing towards the center are called cool core clusters (e.g. NGC 5846 in Figure 1.5); and clusters with no central drop of temperature are called non-cool core clusters. In this thesis, I focus on cool core clusters since their chemical abundances can be relatively well constrained. Their centrally peaked surface brightness profiles are suitable for grating spectrometers like RGS. Due to the deep gravitational potential well, within some sufficient large radius, a relaxed massive cluster can be considered as a "closed-box", namely all the baryons are conserved. This conservation also

[1]Smaller aggregates of galaxies are referred to as groups of galaxies or galaxy groups.

applies to metals in the ICM that are directly observed in X-rays.

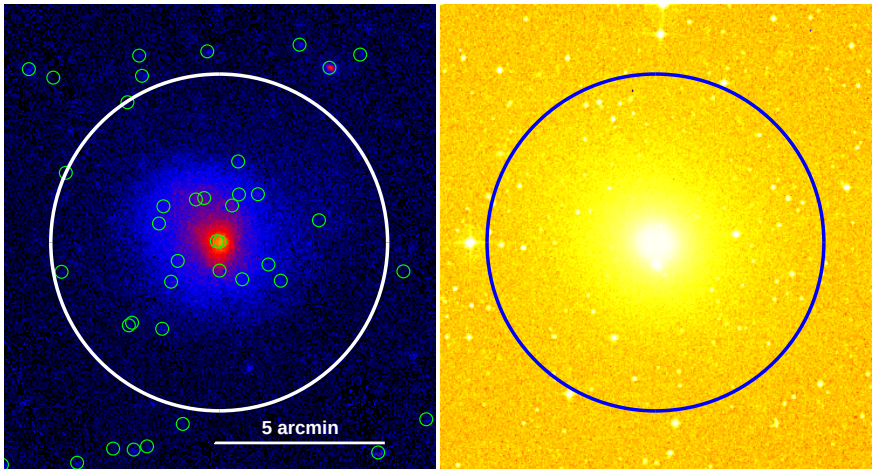

Figure 1.5: *Left*: X-ray image of NGC 5846 from *XMM-Newton*. The small green circles indicate X-ray point sources in the field of view. The white circle has a radius of 5 arcmin. The corresponding physical scale is 36 kpc or $0.1\ r_{500}$, where r_{500} is the radius within which the plasma mass density is 500 times the critical density of the Universe at the redshift of the source. *Right*: Optical image from the Digital Sky Survey (DSS).

Metals in the ICM are originally synthesized by different stellar populations in the member galaxies. Throughout the evolution of the galaxy cluster, different metal transportation mechanisms working on different size-scales and time-scales redistribute these metals from the interstellar medium (ISM) into the ICM (for a review, see Schindler & Diaferio 2008).

Almost every star, except for the least massive ones, contributes to the chemical enrichment of the ICM. Asymptotic giant branch (AGB) stars are low- and intermediate mass stars with $M_* \in (0.9,\ 7)\ \mathrm{M}_\odot$ undergoing the last nuclear burning phase. In this phase, a complex interplay of nucleosynthesis and mixing alters the chemical composition of the stellar atmosphere Karakas (2010). The stellar envelope is enriched with products of hydrogen and helium burning, and heavy elements produced by the slow neutron capture process (i.e., the s process). Metals, especially C and N, are eventually expelled into the ISM via a slow stellar wind.

Massive stars in the mass range of $M_* \in (11,\ 140)\ \mathrm{M}_\odot$ undergo Fe core collapse at the end of their evolution and become Type II and Ib/c supernovae unless the entire star collapses into a black hole with no mass ejection (Nomoto et al. 2013). Hence, core-collapse supernovae (SNcc) products, especially α elements from O to Mg (Figure 1.6), are released into the ISM.

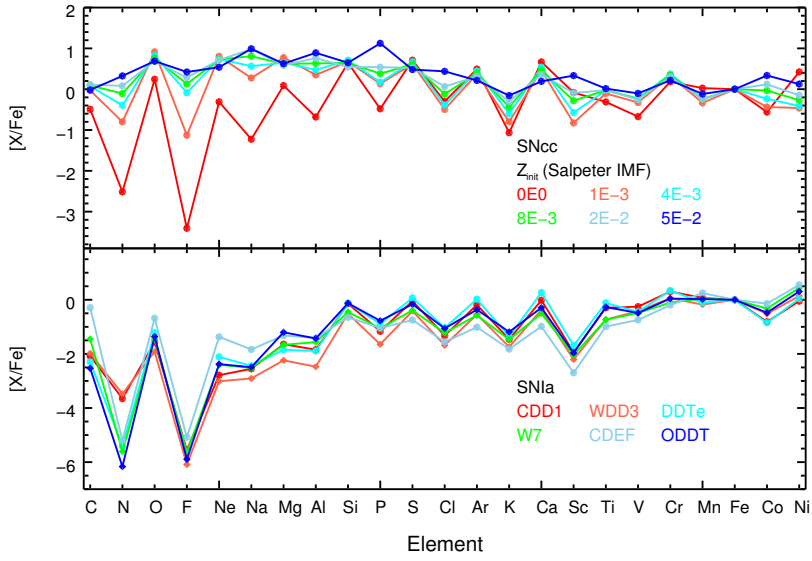

Figure 1.6: *Upper*: IMF weighted yields of core-collapse supernovae (SNcc) with the Salpeter IMF assumed for the progenitor stars. Odd-Z elements like N, Na, and Al are very sensitive to the initial metallicity ($Z_{\rm init}$) of the progenitor stars. *Lower*: Yields of Type Ia supernovae (SNIa) for selective explosion models. Compared to SNcc, elements lighter than Si are significantly less produced by SNIa.

If very massive stars with mass between 140 $\mathrm{M}_\odot$ and 300 $\mathrm{M}_\odot$ do not lose much mass, they undergo thermonuclear explosions triggered by pair-creation instability (PISNe, Barkat et al. 1967). Such events disrupt the progenitors thoroughly without forming a black hole and thus eject a large amount of heavy elements, especially ^{56}Ni (e.g. Heger & Woosley 2002; Umeda & Nomoto 2002) (see also the upper panel of Figure 1.6 with $Z_{\rm init} = 0$).

Degenerate stars in a binary system also contribute to the metal content of the ICM via Type Ia supernovae (SNIa). It is possible that SNIa from different channels (i.e. single- or double-degenerate, super- or sub-Chandrasekhar limit, and deflagration or detonation, Iwamoto et al. 1999; Livio 2000; Maeda et al. 2010) all play a role in the chemical enrichment. SNIa are the main metal factory of Fe-peak elements such as Cr, Mn, Fe and Ni (Figure 1.6).

In many cases, merely the iron abundance in the ICM can be well constrained via the prominent Fe XXVI Lyα and/or Fe XXV He-like triplets. Nonetheless, for bright nearby cool-core clusters, elemental abundances of α elements and Fe-peak elements can be relatively well constrained, especially in terms of abundance ratios

with respect to Fe. These time-integrated abundance ratios are footprints of different enrichment channels (AGBs, SNcc, SNIa).

Assuming that the observed elemental abundances in the ICM are consistent ($\lesssim 20$ %) with the proto-solar abundance (Lodders & Palme 2009), Figure 1.7 illustrates a possible scenario of the chemical enrichment of the ICM. Under a standard Salpeter (Salpeter 1955) initial mass function (IMF, $\xi(M_\star) \propto M_\star^{-2.35}$), progenitor stars with initial metallicity $Z_{\rm init} = 0.008$ enrich C and N mainly via the AGB channel, with a minor contribution from the core-collapse supernovae (SNcc) channel. On the contrary, the enrichment of O to Al is dominated by SNcc. The number of low- and intermediate massive stars (progenitors of AGBs) that contribute to the enrichment with respect to the total number of AGBs and SNcc progenitors is large, $r^{\rm li} = 87 \pm 18$. For elements heavier than Al, Type Ia supernovae start to play a role. In this exercise, we assume the WDD3[2] model (Iwamoto et al. 1999) for SNIa. The number fraction of SNIa ($f^{\rm Ia}$) with respect to the total number of SNIa and SNcc that contributes to the enrichment is (22.3 ± 2.1) %.

From the observational point of view, it is not trivial to interpret the chemical enrichment of the ICM. First, imperfect instruments can also lead to biased abundances. For instance, the European Photon Imaging Camera on board *XMM-Newton* has two sets of CCD (charge-coupled device) arrays: pn and mos. The Ni abundance in the ICM measured by pn and mos can differ up to 60 % (e.g. Figure 6 in Mernier et al. 2016a). The next generation of instruments, like the Soft X-ray Spectrometer (SXS), a calorimeter type of spectrometer, on the *Hitomi* satellite can certainly improve the accuracy of the abundance measurement (Hitomi Collaboration et al. 2017a).

Second, imperfect plasma models can also lead to an incorrect abundance determination. For instance, as shown in de Plaa et al. (2017), inaccurate radiative recombination data implemented in the plasma model can lead to biased O/Fe ratio up to 50 %. Even the state-of-the-art atomic codes can lead to different abundance measurements (Hitomi Collaboration et al. 2017b). More accurate atomic data and plasma models are definitely required.

Third, stellar yields of AGBs, SNcc and SNIa are also not perfect. Current stellar yields are more accurate for elements (e.g. C, N, O, Mg, Si and Fe) observed in optical in galactic chemical evolution studies (e.g., Romano et al. 2010). The accuracy on the yields table of other elements like Ne, P, Ar, and K needs to be

[2] A delayed-detonation explosion scenario with the deflagration to detonation density of 3×10^7 g cm^{-3}, readers are refer to Iwamoto et al. (1999) for more details.

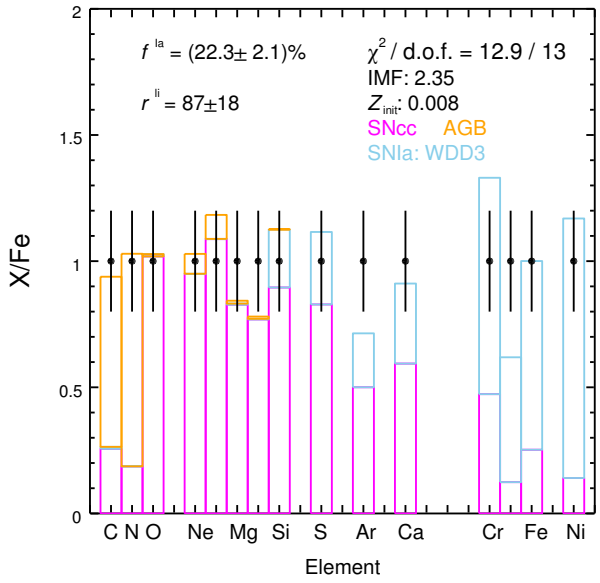

Figure 1.7: Illustration of chemical enrichment. The data points correspond to solar abundance with artificial 20% measurement uncertainties. Metals are enriched via AGBs, SNcc and SNIa. The initial mass function (IMF) of the stellar progenitors is assumed to be follow a power law $\propto M_{\star}^{-\alpha}$ with $\alpha = 2.35$ (Salpeter 1955). The initial metallicity ($Z_{\rm init}$) of the stellar population is 0.008. The number of low- and intermediate massive stars (progenitors of AGBs) that contributes to the enrichment with respect to the total number of AGBs and SNcc progenitors $r^{\rm li} = 87 \pm 18$. The WDD3 model (Iwamoto et al. 1999) is assumed here for the enrichment by SNIa. The number of SNIa that contribute to the enrichment with respect to the total number of SNIa and SNcc $f^{\rm Ia} = (22.3 \pm 2.1)\%$.

checked with observations in X-ray and/or optical.

There are more questions to be addressed for future studies: (1) Whether the IMF and/or initial metallicity is universal? (2) What is the role of hypernova in chemical enrichment? (3) What is the role of pre-enrichment by fast rotating very massive stars via stellar winds? (4) How does chemical enrichment evolve over cosmic time?

1.4. Plasma code and atomic data

Evidently, a suitable plasma code is the prerequisite of interpreting the observed high-resolution X-ray spectra with physical models. Only a handful of plasma codes are available (see also Kaastra et al. 2008, for a review):

1. The SPEX spectral fitting package[3] (Kaastra et al. 1996) has evolved from work by Mewe et al. in 1970s, including the MEKAL (named after MEwe, KAastra & Liedahl) code. The latest version is v3.04. Readers are referred to Section 1 of the SPEX manual[4] for a detailed timeline from MEKAL to the latest version of SPEX. Plasma models provided by SPEX cover various astrophysical scenarios, such as collisional ionization equilibrium in stellar coronae and intracluster media, photoionization equilibrium around black holes, non-equilibrium ionization in supernova remnant and charge exchange recombination at the interface between hot and cold plasmas.

2. AtomDB (Atomic DataBase)[5] is an atomic database useful for X-ray plasma spectral modeling. It includes APEC (Astrophysical Plasma Emission Code Smith et al. 2001), which has evolved originally from the work by Raymond & Smith (1977) for collisional ionization equilibrium, as well as NEI for non-equilibrium ionization. The latest version is v3.0.9. Note that APEC and NEI codes are used through spectral fitting packages like XSPEC (Arnaud 1996).

3. XSTAR[6] is a code for calculating the physical conditions and emission spectra of photoionized plasmas. It has evolved from the early work by Kallman & McCray (1982) and the latest version is v2.39.

4. Cloudy[7] is a code for simulating conditions in interstellar matter under a broad range of conditions, including photoionization equilibrium and collisional ionization equilibrium. The latest version (v17.00) was released in 2017 (Ferland et al. 2017).

5. CHIANTI[8] (named after the wine region near Firenze Landi et al. 2006) has evolved from early work by Landini & Monsignori Fossi (1970), focusing on solar spectral analysis. The package performs collisional ionization equilibrium calculation and the latest version is v8.0 (Del Zanna et al. 2015).

All these codes require an extensive atomic database covering relevant atomic processes such as collisional ionization, photoionization, radiative recombination, dielectronic recombination, charge exchange recombination, collisional (de-)excitation,

[3] https://www.sron.nl/astrophysics-spex
[4] http://var.sron.nl/SPEX-doc/manualv3.04.00.pdf
[5] http://www.atomdb.org/
[6] https://heasarc.gsfc.nasa.gov/lheasoft/xstar/xstar.html
[7] http://www.nublado.org/
[8] http://www.chiantidatabase.org/

and bremsstrahlung, etc. The leading concern is that incomplete and imperfect atomic data/code can lead to inaccurate plasma diagnostics, thus influencing our understanding of the Universe. Another issue is that code developers need to find the balance among evergrowing atomic data (tens of gigabytes at the moment) and computation time.

Over the past few years, the SPEX development team has made significant updates to atomic data and code for all built-in plasma models. Gu et al. (2016) introduced the new charge exchange model (CX). Mehdipour et al. (2016) described the updated the photoionization model (PION) and compared it to other population photoionization codes. Mao & Kaastra (2016, i.e., **Chapter 2**) and Mao et al. (2017a, i.e., **Chapter 3**) updated the radiative recombination related data, Urdampilleta et al. (2017) updated the inner-shell ionization data and revised accordingly the charge stage distribution of the collisional ionization equilibrium (CIE). Mao et al. (2017b, i.e., **Chapter 4**) demonstrated how the updated photoionization model (PION) allows density diagnostics with metastable absorption lines in Be-like to C-like isoelectronic sequences. Kaastra et al. (2017) highlighted the astrophysical applications of the updated plasma code in the context of the current and future generation of X-ray spectroscopy observatories.

Nonetheless, there are unresolved issues. Spectra that contain Fe XVII emission features, for instance, are poorly fitted even with the best collisional ionization plasma models (Bernitt et al. 2012). A significant portion of atomic data of many-electron ions (e.g. O-like isoelectronic sequence) are still lacking in the updated atomic database of the SPEX code.

1.5. This thesis

This thesis includes publications where I did the majority of the work and writing. All the coauthors have reviewed, discussed and commented on the manuscripts. In particular, prof. dr. N. R. Badnell made important contribution on publishing his AUTOSTRUCTURE and ADASRR codes and providing some insights to his code in Chapter 3. In Chapters 4 to 6, prof. dr. J. S. Kaastra and dr. M. Mehdipour made important contributions on leading the multi-wavelength observational proposals as primary investigators and reducing the data. In Chapter 7, dr. J. de Plaa is the primary investigator of *XMM-Newton* proposal and dr. F. Mernier contributed on the EPIC abundance measurements of NGC 5044. A full list of publications is available as the penultimate part of this thesis.

This thesis starts with updates of radiative recombination data in the spectral

analysis package SPEX, where various plasma models are built on a single atomic database. The updated plasma models are then used to better understand the physics of circumnuclear media and the nitrogen enrichment in the intracluster media.

Radiative recombination (RR) is a fundamental atomic process where a positively charged ion captures a free electron to one of its bound orbits. A photon is emitted during the process with its energy equal to the kinetic energy of the free electron plus the binding energy of the newly-recombined electron. Since the kinetic energy is not quantized, this forms a continuous emission. Furthermore, the newly-recombined electron can lead to line emission via cascades to the ground level.

Previously, the RR rate coefficients (i.e., the electron capture rates per ion) in SPEX were approximated with a power law. In **Chapter 2**, I propose a slightly more complicated math function, which matches much better ($\lesssim 5\%$) the state-of-the-art RR rate coefficients (Badnell 2006). While the RR rate coefficients are available, the associated electron energy loss rates are lacking, except for H-like ions and He I. The total electron energy loss rates due to RR are required to solve the thermal equilibrium in photoionized plasma modeling. Therefore, in **Chapter 3**, I update the AUTOSTRUCTURE and ADASRR codes (Badnell 2006) to calculate detailed electron energy loss rates systematically. This is the first time the electron energy loss rates due to RR of He-like to Ne-like ions have been calculated.

For photoionized plasmas, these electron energy loss rates due to radiative recombination are essential for thermal equilibrium calculations, which assume a local balance between the energy gain and loss. A systematic study of density diagnostics using absorption lines from metastable levels is also lacking for photoionized plasmas. Therefore, I carry out such kind of study in **Chapter 4**.

With the self-consistent PhotoIONization (PION) model in the SPEX code, we are able to calculate detailed level populations, including the ground and metastable levels. This enables us to determine under what physical conditions the metastable levels are significantly populated. Observationally, due to the lack of sufficient spectral resolution and limited photon collecting area, density diagnostics of the spectra obtained with the current generation of X-ray spectrometers are not very effective. For instance, I reanalyze the high-resolution grating spectra of NGC 5548 observed with Chandra in January 2002 using a set of PION components to account for the ionized outflow. I derive lower (or upper) limits of plasma density in five out of six PION components based on the presence (or absence) of the metastable

absorption lines. For NGC 5548, it is the first time plasma density of the ionized outflows in X-ray has been constrained using metastable absorption lines. Future missions like *Arcus* (Smith et al. 2016) will allow us to better constrain the density thus the distance and kinetic power of AGN outflows (Kaastra et al. 2017).

Photoionized plasmas in AGN are manifest not only in absorption features but also in emission features, such as the X-ray broad and narrow emission features observed in Seyfert galaxies. It is easier to study the soft X-ray emission features in Seyfert 2 galaxies (e.g., Kinkhabwala et al. 2002, for NGC 1068) because the AGN continuum is blocked by the dusty torus. But there is a growing number of studies of the soft X-ray emission features in Seyfert 1 galaxies, either because the source was caught in a low flux state (e.g., Nucita et al. 2010, for NGC 4051), or due to the newly discovered heavy obscuration of the soft X-ray continuum (Kaastra et al. 2014; Mehdipour et al. 2017).

In **Chapter 5**, the X-ray narrow emission features in the archetypal Seyfert 1 galaxy NGC 5548 are studied. I find that the X-ray narrow emission features in NGC 5548 can be described by a two-phase photoionized plasma with different ionization parameters and kinematics, and no further absorption by the warm absorber components. The X-ray and optical narrow emission line region are most likely the same multi-phase photoionized plasma. The X-ray narrow emission line region is not the counterpart of the UV/X-ray absorber outside the line of sight because their distances and kinematics are not consistent. In short, our understanding of the relations among different circumnuclear media components has been advanced.

Similar to NGC 5548, our *Swift* monitoring programme triggered two joint *XMM-Newton*, *NuSTAR* and HST observations on 11 and 21 December 2016 targeting NGC 3783, as its soft X-ray continuum was also heavily obscured. Consequently, emission features, including the O VII radiative recombination continuum, stand out above the diminished continuum. In **Chapter 6**, I focus on the photoionized emission features in the December 2016 RGS spectra, and compare them to the time-averaged RGS spectrum obtained in 2000–2001 when the continuum was unobscured. Two distinct photoionized components are required to account for the narrow emission features. The narrow emission features are weakly varying between 2000–2001 and December 2016. We also find a statistically significant broad emission component in the time-averaged RGS spectrum in 2000–2001. This broad emission component is significantly less prominent in December 2016. I demonstrate that the weakening might be due to the extra screening by the obscurer, indicating that the obscurer is beyond the X-ray broad-line region.

1

While previous chapters are about photoionized plasma modeling, the last chapter focuses on collisional ionized plasma modeling. The chemical abundance measurement of collisionally ionized plasmas in clusters and groups of galaxies depends on the line emissivity predicted by the plasma model. Therefore, more accurate radiative recombination data lead to more accurate abundance measurement (de Plaa et al. 2017; Mernier et al. 2016a) and thus their origins.

Previous studies (e.g., Mernier et al. 2016b) have established that α elements (e.g., O, Ne, and Mg) are mainly produced in massive stars as they explode as core-collapse supernovae, while the Fe-peak elements (e.g., Cr, Mn, Fe, and Ni) are produced in single- and/or double-degenerate stars as they explode as Type Ia supernovae. In **Chapter 7**, I investigate the nitrogen enrichment in the CHEmical Evolution Rgs Sample of ellipticals, groups and clusters of galaxies. Under a standard initial mass function, low- and intermediate-mass stars are the main metal factory of nitrogen in the hot X-ray halos of groups and clusters of galaxies. In addition, I point out that the initial metallicity of stellar populations is more sensitive to abundances of odd-Z elements (N, Na, and Al). Future missions like the X-ray Astronomy Recovery mission (*XARM*) are required to have accurate abundances of these elements.

References

Arav, N., Chamberlain, C., Kriss, G. A., et al. 2015, A&A, 577, A37
Arnaud, K. A. 1996, in Astronomical Society of the Pacific Conference Series, Vol. 101, Astronomical Data Analysis Software and Systems V, ed. G. H. Jacoby & J. Barnes, 17
Badnell, N. R. 2006, ApJS, 167, 334
Barkat, Z., Rakavy, G., & Sack, N. 1967, Physical Review Letters, 18, 379
Bennert, N., Jungwiert, B., Komossa, S., Haas, M., & Chini, R. 2006a, A&A, 459, 55
Bennert, N., Jungwiert, B., Komossa, S., Haas, M., & Chini, R. 2006b, A&A, 456, 953
Bernitt, S., Brown, G. V., Rudolph, J. K., et al. 2012, Nature, 492, 225
Böhringer, H. & Werner, N. 2010, A&A Rev., 18, 127
Brinkman, A. C., Gunsing, C. J. T., Kaastra, J. S., et al. 2000, ApJ, 530, L111
Canizares, C. R., Davis, J. E., Dewey, D., et al. 2005, PASP, 117, 1144
Collinge, M. J., Brandt, W. N., Kaspi, S., et al. 2001, ApJ, 557, 2
de Plaa, J., Kaastra, J. S., Werner, N., et al. 2017, A&A, 607, A98
Del Zanna, G., Dere, K. P., Young, P. R., Landi, E., & Mason, H. E. 2015, A&A, 582, A56
den Herder, J. W., Brinkman, A. C., Kahn, S. M., et al. 2001, A&A, 365, L7
Ebrero, J., Kaastra, J. S., Kriss, G. A., et al. 2016, A&A, 587, A129
Fabian, A. C. 2012, ARA&A, 50, 455
Ferland, G. J., Chatzikos, M., Guzmán, F., et al. 2017, , 53, 385
Gu, L., Kaastra, J., & Raassen, A. J. J. 2016, A&A, 588, A52

Haardt, F. & Maraschi, L. 1991, ApJ, 380, L51
Haardt, F. & Maraschi, L. 1993, ApJ, 413, 507
Heger, A. & Woosley, S. E. 2002, ApJ, 567, 532
Hitomi Collaboration, Aharonian, F., Akamatsu, H., et al. 2017a, Nature, 551, 478
Hitomi Collaboration, Aharonian, F., Akamatsu, H., et al. 2017b, ArXiv e-prints
Iwamoto, K., Brachwitz, F., Nomoto, K., et al. 1999, ApJS, 125, 439
Kaastra, J. S., Detmers, R. G., Mehdipour, M., et al. 2012, A&A, 539, A117
Kaastra, J. S., Gu, L., Mao, J., et al. 2017, Journal of Instrumentation, 12, C08008
Kaastra, J. S., Kriss, G. A., Cappi, M., et al. 2014, Science, 345, 64
Kaastra, J. S., Mewe, R., & Nieuwenhuijzen, H. 1996, in UV and X-ray Spectroscopy of Astrophysical and Laboratory Plasmas, ed. K. Yamashita & T. Watanabe, 411–414
Kaastra, J. S., Paerels, F. B. S., Durret, F., Schindler, S., & Richter, P. 2008, Space Sci. Rev., 134, 155
Kaastra, J. S., Raassen, A. J. J., Mewe, R., et al. 2004, A&A, 428, 57
Kallman, T. R. & McCray, R. 1982, ApJS, 50, 263
Karakas, A. I. 2010, MNRAS, 403, 1413
Kellermann, K. I., Sramek, R., Schmidt, M., Shaffer, D. B., & Green, R. 1989, AJ, 98, 1195
King, A. L., Miller, J. M., & Raymond, J. 2012, ApJ, 746, 2
King, A. R. & Pounds, K. A. 2003, MNRAS, 345, 657
Kinkhabwala, A., Sako, M., Behar, E., et al. 2002, ApJ, 575, 732
Kormendy, J. & Ho, L. C. 2013, ARA&A, 51, 511
Koshida, S., Minezaki, T., Yoshii, Y., et al. 2014, ApJ, 788, 159
Krolik, J. H., McKee, C. F., & Tarter, C. B. 1981, ApJ, 249, 422
Landi, E., Del Zanna, G., Young, P. R., et al. 2006, ApJS, 162, 261
Landini, M. & Monsignori Fossi, B. C. 1970, A&A, 6, 468
Livio, M. 2000, in Type Ia Supernovae, Theory and Cosmology, ed. J. C. Niemeyer & J. W. Truran, 33
Lodders, K. & Palme, H. 2009, Meteoritics and Planetary Science Supplement, 72, 5154
Maeda, K., Röpke, F. K., Fink, M., et al. 2010, ApJ, 712, 624
Maiolino, R. & Rieke, G. H. 1995, ApJ, 454, 95
Mao, J. & Kaastra, J. 2016, A&A, 587, A84
Mao, J., Kaastra, J., & Badnell, N. R. 2017a, A&A, 599, A10
Mao, J., Kaastra, J. S., Mehdipour, M., et al. 2017b, A&A, 607, A100
Mason, K. O., Breeveld, A., Much, R., et al. 2001, A&A, 365, L36
McKernan, B., Yaqoob, T., George, I. M., & Turner, T. J. 2003, ApJ, 593, 142
Mehdipour, M., Kaastra, J. S., Kriss, G. A., et al. 2017, A&A, 607, A28
Mehdipour, M., Kaastra, J. S., Kriss, G. A., et al. 2016, A&A, 588, A139
Mernier, F., de Plaa, J., Pinto, C., et al. 2016a, A&A, 592, A157
Mernier, F., de Plaa, J., Pinto, C., et al. 2016b, A&A, 595, A126
Nandra, K., Barret, D., Barcons, X., et al. 2013, ArXiv e-prints
Netzer, H. 2015, ARA&A, 53, 365
Nicastro, F., Fiore, F., Perola, G. C., & Elvis, M. 1999, ApJ, 512, 184
Nomoto, K., Kobayashi, C., & Tominaga, N. 2013, ARA&A, 51, 457
Nucita, A. A., Guainazzi, M., Longinotti, A. L., et al. 2010, A&A, 515, A47
Osterbrock, D. E. 1981, ApJ, 249, 462
Padovani, P., Alexander, D. M., Assef, R. J., et al. 2017, A&A Rev., 25, 2

Peterson, B. M., Ferrarese, L., Gilbert, K. M., et al. 2004, ApJ, 613, 682
Porquet, D., Dubau, J., & Grosso, N. 2010, Space Sci. Rev., 157, 103
Raymond, J. C. & Smith, B. W. 1977, ApJS, 35, 419
Romano, D., Karakas, A. I., Tosi, M., & Matteucci, F. 2010, A&A, 522, A32
Salpeter, E. E. 1955, ApJ, 121, 161
Schindler, S. & Diaferio, A. 2008, Space Sci. Rev., 134, 363
Schmidt, M. 1963, Nature, 197, 1040
Schurch, N. J., Warwick, R. S., Griffiths, R. E., & Kahn, S. M. 2004, MNRAS, 350, 1
Seyfert, C. K. 1943, ApJ, 97, 28
Silva, C. V., Uttley, P., & Costantini, E. 2016, A&A, 596, A79
Smith, R. K., Abraham, M. H., Allured, R., et al. 2016, in Proc. SPIE, Vol. 9905, Space Telescopes and Instrumentation 2016: Ultraviolet to Gamma Ray, 99054M
Smith, R. K., Brickhouse, N. S., Liedahl, D. A., & Raymond, J. C. 2001, ApJ, 556, L91
Strüder, L., Briel, U., Dennerl, K., et al. 2001, A&A, 365, L18
Takahashi, T., Mitsuda, K., Kelley, R., et al. 2014, in Proc. SPIE, Vol. 9144, Space Telescopes and Instrumentation 2014: Ultraviolet to Gamma Ray, 914425
Tarter, C. B., Tucker, W. H., & Salpeter, E. E. 1969, ApJ, 156, 943
Umeda, H. & Nomoto, K. 2002, ApJ, 565, 385
Urdampilleta, I., Kaastra, J. S., & Mehdipour, M. 2017, A&A, 601, A85
Weedman, D. W. 1973, ApJ, 183, 29